Photochemistry of $HgBr_2$ in methanol investigated using time-resolved X-ray liquidography

Sunhong Jun,[a] Jae Hyuk Lee,[a] Jeongho Kim,[a] Joonghan Kim,[a] Kyung Hwan Kim,[a] Qingyu Kong,[b] Tae Kyu Kim,[c] Manuela Lo Russo,[d] Michael Wulff*[d] and Hyotcherl Ihee*[a]

Received 29th January 2010, Accepted 18th May 2010
DOI: 10.1039/c002004d

We investigate the photoinduced dissociation of $HgBr_2$ in methanol and the ensuring structural dynamics of the photo-products over a time span from 100 ps to 1 μs after photolysis at 267 nm by using time-resolved X-ray liquidography (TRXL). By making use of the atomic-level structural sensitivity of X-ray scattering and the superb 100 ps time resolution of X-ray pulses from a 3rd-generation synchrotron, the structural dynamics of a chemical reaction in solution can be directly monitored. The measured time-dependent X-ray solution scattering signals, analyzed using global-fitting based on DFT calculations and MD simulations, show that photoexcited $HgBr_2$ dissociates *via* both two-body (HgBr + Br) and three-body (Hg + Br + Br) dissociation pathways with a ~2 : 1 branching ratio. Following dissociation, the photoproducts recombine *via* three reactions involving Br species: (1) Hg + Br, (2) HgBr + Br, and (3) Br + Br. The associated rate constants and branching ratios are determined from the global-fitting analysis. Also, we examine the energy dissipation from reacting solute molecules and relaxation of excited molecules to solvent bath accompanying the temperature rise of 0.54 K. Compared to a previous TRXL study of the photodissociation of HgI_2, the results of this work suggest that the photodissociation pathway of $HgBr_2$ is different from that of HgI_2, which dissociates predominantly *via* two-body dissociation, at least to within the currently available time resolution of ~100 ps. In addition, the error analysis of the fit parameters used in the global-fitting are discussed in detail with a comparison of various error estimation algorithms.

1. Introduction

Over the last century, mercuric halides, HgX_2 (X = Cl, Br and I), and their photodissociation dynamics have attracted much interest due to their optical and electronic properties.[1–14] Their simple triatomic molecular structure, high photochemical reactivity, fast recombination rates, and the presence of heavy atoms have made them a good model system for studying ultrafast photochemistry.[15] Accordingly, the photodissociation of HgX_2 in the gas phase has been the subject of many spectroscopic and theoretical studies. For example, Zewail and coworkers have studied the photoinduced reaction dynamics of HgI_2 using femtosecond transient absorption and fluorescence spectroscopy, discovering that the reaction proceeds through two-body dissociation of $HgI_2 \rightarrow HgI + I$ along reaction coordinates consisting of two vibrational modes.[16,17] Moreover, the branching dynamics of HgI_2 on a saddle point on the potential energy surface (PES) were investigated using femtosecond mass spectrometry[18,19] and theoretical quantum chemistry.[20,21] In addition to the fundamental interest, the discovery of their electronic-transition lasing action has inspired technological interest with the potential applications in blue-green laser system.[22,23] Photodissociation of HgX_2 induces the formation of HgX (X = Cl, Br, I) radical species, of which the $B^2\Sigma^+ \rightarrow X^2\Sigma^+$ transition[24–32] accounts for strong fluorescence emission relevant for lasing application.

In contrast to the intense investigations of mercuric halides in the gas phase, the study of the photodissociation reaction of HgX_2 in solution is relatively limited. Previously, the photodissociation dynamics of HgI_2 (in ethanol and DMSO) and $HgBr_2$ (in CH_3CN and DMSO) in the solution phase have been studied using femtosecond transient absorption spectroscopy, elucidating the rovibrational wave-packet motion as well as solvation dynamics on the timescale of tens of picoseconds (ps).[33–42] However, more comprehensive understanding of the reaction mechanism in the solution phase is needed, in particular, branching ratios and recombination dynamics of photodissociated species spanning the picosecond to microsecond timescale.

Although time-resolved optical spectroscopy has had much success in probing ultrafast photoreaction dynamics, it is limited in resolving detailed mechanism of the reaction due to the nature of its probing target: optical spectroscopy is sensitive to the population of specific electronic or vibrational states but it cannot obtain direct information on the molecular

[a] *Center for Time-Resolved Diffraction, Department of Chemistry, Graduate School of Nanoscience & Technology (WCU), KAIST, Daejeon, 305-701, Republic of Korea. E-mail: hyotcherl.ihee@kaist.ac.kr*
[b] *Société Civile Synchrotron SOLEIL, L'Orme des Merisiers Saint-Aubin, BP 48, 91192 Gif-sur-Yvette Cedex, France*
[c] *Department of Chemistry and Institute of Functional Materials, Pusan National University, Busan, 609-735, Republic of Korea*
[d] *European Synchrotron Radiation Facility, 6 Rue Jules Horowitz, BP 220, 38043 Grenoble Cedex, France. E-mail: wulff@esrf.fr*

structure. In that regard, time-resolved X-ray liquidography (TRXL), also known as time-resolved X-ray solution scattering, is an ideal tool for investigating reaction dynamics because X-ray scattering is sensitive to the global molecular structure. Over the last decade, the TRXL has been established as an effective tool to monitor the progress of chemical reactions in solution,[43,44] capturing transient structures in solution-phase reactions of small organic/inorganic molecules,[45–54] nanoparticles,[55–57] and biological macromolecules[58–60] with an atomic-scale spatial precision and a time resolution down to 100 ps.

Previously, TRXL was applied to one of the mercuric halides, HgI_2 dissolved in methanol,[46] revealing the dissociation pathways, solvent energetics, and the transient structures of intermediates. In particular, it was found that the primary reaction pathway in solution is two-body dissociation into HgI and I in contrast to the gas-phase reaction that involves both two-body ($HgI_2 \rightarrow HgI + I$) and three-body dissociation ($HgI_2 \rightarrow Hg + I + I$).[19] In this work, we applied TRXL to another mercuric halide system in solution, $HgBr_2$ in methanol, to investigate the dynamics and mechanism of its photodissociation reaction. In particular, we examine the primary reaction pathways by identifying the structure of the transient species and determine the rates of the reactant recombination and heat dissipation. Also, we investigated the effect of chemical substitution on the reaction dynamics by comparison with the HgI_2 dynamics.

To determine the primary reaction pathways for the dissociation of photoexcited $HgBr_2$, we considered four possible reaction channels (see Fig. 1A for details):

$$HgBr_2^* \rightarrow HgBr + Br \quad (1)$$

$$HgBr_2^* \rightarrow Hg + Br + Br \quad (2)$$

$$HgBr_2^* \rightarrow Hg + Br_2 \quad (3)$$

$$HgBr_2^* \rightarrow HgBr - Br' \quad (4)$$

Based on the previous experimental and theoretical studies of mercuric halides,[16,17,19,21,36,46] the most plausible pathway is pathway (1), where the BrHg–Br bond breaks along the reaction coordinate of an asymmetric stretching of BrHgBr, resulting in bond rupture into HgBr and Br. Two-body dissociation of $HgBr_2$ has already been observed in solution phase using femtosecond absorption spectroscopy.[36] Another candidate for the primary reaction is pathway (2), where both Hg–Br bonds of $HgBr_2$ break along a symmetric stretching reaction coordinate to produce one Hg and two Br atoms. This three-body photodissociation of $HgBr_2$ was also observed in the gas phase by femtosecond mass-spectrometry.[19] Besides these two pathways, we considered the pathways producing Hg and Br_2 (pathway (3))[21] or the HgBr–Br′ isomer (pathway (4)). Upon photoexcitation by 266 nm laser light, the $HgBr_2$ molecule in the ground state is vertically excited to an excited state lying higher in energy by 448.2 kJ mol^{-1}. From a thermodynamic point of view, all four candidate pathways (1) to (4) are plausible because the primary photoproducts of all the pathways lie lower in energy than the initially excited state, as can be seen in the DFT calculations (Fig. 1B). For comparison, the relative energies of the products from

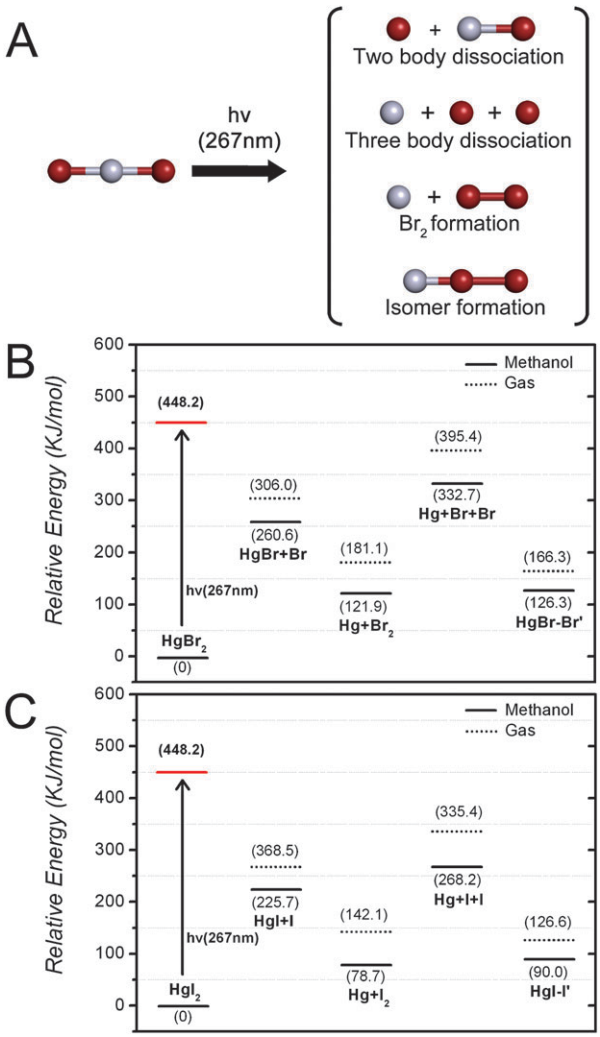

Fig. 1 (A) Four candidate reaction pathways of $HgBr_2$ photodissociation in methanol initiated by the 266 nm laser wavelength excitation used in this study. Hg and Br atoms are represented in grey and red respectively. Relative energies of the photodissociation products of (B) $HgBr_2$ and (C) HgI_2 in methanol (solid) and in the gas phase (dashed). All values were calculated by DFT with the PBE0 functional. Basis sets for Hg, Br and I were all aug-cc-pVTZ-PP RECP. The CPCM method was applied to describe the solvent effects. The results of the calculation show that all four reaction channels are possible thermodynamically because the products of all the reaction channels lie lower than the initially excited state, $HgBr_2$* or HgI_2*.

corresponding reaction pathways of HgI_2 photodissociation are shown in Fig. 1C. It can be seen that the product states of HgI_2 and $HgBr_2$ photodissociation have the same energy ordering. From our TRXL measurements and theoretical analysis, we identify the structures of the transient intermediates and examine the major reaction pathways in the photodissociation of $HgBr_2$.

2. Experimental

2.1 Time-resolved X-ray liquidography

The TRXL is a pump–probe method that employs the laser pulse as a pump and the hard X-ray pulse as a probe.

A reaction of sample molecules is initiated by a laser pulse and the progress of the reaction is monitored by a time-delayed X-ray pulse scattered (or diffracted) off the sample. The obtained time-dependent scattering patterns contain the information on the transient structure of reacting molecules. By analyzing the scattering signals measured at various pump–probe time delays, the reaction dynamics can be revealed. For the analysis, the experimental curves are fitted against theoretical curves by a least-square fitting method. The theoretical scattering curves of molecular species involved in the reaction are generated based on the molecular structure calculated by high-level DFT calculation and pair distribution functions from MD simulation. A more detailed description is given in our review articles.[43,44]

2.2 Experimental methods and materials

The TRXL experiments were performed using beamline ID09B at the European Synchrotron Radiation Facility (ESRF). The detailed setup of the TRXL experiment is described elsewhere.[43–46,48–50] Briefly, a typical pump–probe scheme with optical pump and X-ray probe pulses was adopted to initiate and monitor the chemical reaction, respectively.[61] A 266 nm ultraviolet laser pulse, generated by frequency-tripling the 800 nm output from an amplified Ti:sapphire laser system, was used to trigger the photodissociation reaction of $HgBr_2$. In order to prevent multi-photon excitation, the laser pulse was temporally stretched to ~2 ps by passing it through a fused silica rod of 30 cm length. The laser pulse with 40 μJ per pulse was focused to a diameter of 100 μm at the sample, giving a fluence of 4 mJ mm^{-2}. Subsequently, a time-delayed X-ray pulse was used to probe the progress of the reaction. The X-ray pulse is ~100 ps long with 5×10^8 photons per pulse, and it is quasi-monochromatic with its spectrum peaked at 18.2 keV and of 0.45 keV bandwidth. The X-ray pulse was selected from the 16-bunch filling mode of the synchrotron ring using a synchronized mechanical chopper, and was focused to 100×60 μm^2 on the sample. The temporal overlap between X-ray and laser pulses was monitored by a fast GaAs detector, and the time delay was varied electronically with 5 ps precision. The laser and X-ray pulses were also spatially overlapped in a quasi-parallel geometry with a cross-angle of 10 degrees. The two-dimensional (2D) scattering patterns were collected with an area detector (MARCCD, Mar Systems, 2048 by 2048, 64.3 μm effective pixel size) with a sample-to-detector distance of 40 mm and an exposure time of 15 s. The solution sample was prepared by dissolving $HgBr_2$ (Aldrich, 99.99%) in methanol at 25 mM concentration and was circulated through a high-pressure slit nozzle (0.3 mm slit, Kyburz) to form a liquid jet. The nozzle provides a stable flow of liquid and allows the refreshment of the liquid sample between subsequent laser pulses at a repetition rate of 1 kHz. The solution scattering signals were measured at various time delays between the laser and X-ray pulses (−200 ps, 100 ps, 300 ps, 1 ns, 3 ns, 10 ns, 20 ns, 40 ns, 100 ns, and 1 μs). In addition, the signal at a negative time delay (−3 ns) was measured as a reference for the unexcited sample and was used for obtaining the difference scattering.

2.3 Data processing

The 2D scattering patterns recorded on the CCD detector were azimuthally integrated into one-dimensional intensity curves, $S(q,t)$, as a function of momentum transfer q ($q = (4\pi/\lambda)\sin(\theta)$, where λ is the wavelength of the X-ray, 2θ is the scattering angle and t is the time delay between the laser and X-ray pulses. The curves were averaged and scaled to the total scattering, both elastic and inelastic, from non-excited solvent/solute background in the high q region, where the scattering in insensitive to structural changes. After scaling the intensities, difference-scattering curves were generated by subtracting the reference data measured at −3 ns from the data at other time delays.[62] Then, q is multiplied to $\Delta S(q,t)$ to magnify the intensities at high scattering angles. The correlated difference radial distribution function (RDF), $r\Delta S(r,t)$, which provides radial electron density change as a function of interatomic distance r in real space, was obtained by sine-Fourier-transforming the $q\Delta S(q,t)$ curves:

$$r\Delta S(r,t) = \frac{1}{2\pi^2}\int_0^\infty q\Delta S(q,t)\sin(qr)\exp(-q^2\alpha)\,\mathrm{d}q, \quad (5)$$

where the constant α ($\alpha = 0.03$ $Å^2$) is a damping constant to account for the finite q range in the experiment.

2.4 Data analysis

The treated data curves, $q\Delta S(q,t)$, were analyzed using our home-made algorithm, which is a weighted least-square fitting method that minimizes the chi-square (χ^2) between the experimental data and the model function. Since the experimental $q\Delta S(q,t)$ data at all time delays are related to each other through reaction kinetics, the fitting was done *via* a global-fitting procedure that simultaneously minimizes the total χ^2 at all positive time delays, *i.e.*,

$$\chi^2 = \sum_{j=\text{time delay}} \chi_j^2 \quad (6)$$

and

$$\chi_j^2 = \sum_i \left(\frac{\Delta S_{\text{theory}}(q_i,t_j) - \Delta S_{\text{experimental}}(q_i,t_j)}{\sigma_{i,j}}\right)^2, \quad (7)$$

where $\sigma_{i,j}$ is the standard deviation of the individual scans at a given time delay. The global-fitting parameters were rate constants of various reaction pathways, branching ratios among photoproducts, and the size of laser spot at the sample. The χ^2 was minimized using the MINUIT package written at CERN.[63]

In the fitting analysis, we fit the experimentally measured difference intensities using theoretical difference intensities. The model function for the theoretical difference intensity accounts for three major components contributing to the signal: (i) solute-only term, (ii) solute–solvent cross-term

(called the cage term), and (iii) solvent-only term, as in the following expression:

$$\begin{aligned}\Delta S(q,t) &= \Delta S_{\text{solute-only}}(q,t) + \Delta S_{\text{solute-solvent}}(q,t) \\ &\quad + \Delta S_{\text{solvent-only}}(q,t) \\ &= \Delta S_{\text{solute-related}}(q,t) + \Delta S_{\text{solute-only}}(q,t) \\ &= \frac{1}{R}\left[\sum_k c_k(t)S_k(q) - S_g(q)\sum_k c_k(0)\right] \\ &\quad + \left[\left(\frac{\partial S}{\partial T}\right)_\rho \Delta T(t) + \left(\frac{\partial S}{\partial \rho}\right)_T \Delta\rho(t)\right],\end{aligned} \tag{8}$$

where R is the ratio of the number of solvent molecules to that of solute molecules, k is the index of the solute species (reactants, intermediates and products), $c_k(t)$ is the fraction of k species as a function of time delay t, $S_k(t)$ is the solute-related (that is, solute-only plus the cage components) scattering intensity of species k, $S_g(q)$ is the scattering intensity of the reactants (g = reactants), $(\partial S(q)/\partial T)_\rho$ is the change in the solvent scattering intensity in response to a temperature rise at constant density, $(\partial S(q)/\partial\rho)_T$ is the solvent scattering change with respect to a density change of solvent at constant temperature, and $\Delta T(t)$ and $\Delta\rho(t)$ are the changes in temperature and density of the solvent, respectively, at a time delay t. The $S_k(q)$ were calculated based on results from MD simulation and DFT calculation. The solvent differential functions, $(\partial S(q)/\partial T)_\rho$ and $(\partial S(q)/\partial\rho)_T$, were determined from a separate measurement where pure methanol solvent is vibrationally excited by near-infrared light.[64]

2.5 Density functional theory calculations

The structural information about the solute molecules and their presumed photoproducts was calculated using Density Functional Theory (DFT). We used the PBE0[65] functional as DFT exchange–correlation functional, and all quantum chemical calculations were carried out by the Gaussian03 program.[66] It was found that the PBE0 is well suited for predicting the molecular structure of HgX_n (X = Br and I, n = 1 and 2), giving the bond lengths in good agreement with experimental values obtained in the gas phase.[67] The accuracy of PBE0 for the calculation of HgX_n is comparable to that of CCSD(T), which is the most accurate quantum calculation method. As a basis set, aug-cc-pVTZ-PP small-core relativistic effective core potential (RECP) was used for Hg,[68] Br[69] and I[70] so that relativistic effect of heavy element can be considered. Since this basis set is at a triple zeta level (aug-cc-pVTZ-PP) for the valence space, the molecular structures of $HgBr_n$ and HgI_n can be well described. To account for the solvent effects, we used the conductor-like polarizable continuum model (CPCM)[71] method that effectively works for polar solvents. The structures were fully optimized in the solvent environment and subsequent harmonic vibrational frequencies were calculated for the optimized structures.

2.6 Molecular dynamics simulations

The molecular dynamics (MD) simulations were run using the program MOLDY[72] which has provided good results in previous works.[45–49,62] The so-called H1 methanol model[73] was used to account for solvent environment. The H1 methanol model that assumes each methanol molecule is a rigid body is well suited for predicting the X-ray scattering signal from methanol. For the simulation of the diffraction from the solute in its solvation cage, we used one solute molecule ($HgBr_2$, HgBr, HgBr–Br′, Br, and Br_2) surrounded by 256 methanol molecules in a cubic box of ~26 Å. All simulations were performed at ambient temperature (300 K) with a density of 0.794 g cm^{-3}. The system was equilibrated at 300 K over 200 ps at a constant temperature *via* coupling to a Nose–Hoover thermostat.[74] The time-step was 0.001 ps and the simulations were performed in the NVT ensemble and the trajectories were followed up to 1 ns. The scattered intensity from each molecular configuration was calculated from the atom–atom distribution functions $g_{\alpha\beta}(r)$ using our own programs and tabulated atomic form factors.

3. Results and discussion

3.1 X-ray solution scattering signal of $HgBr_2$ in methanol

In Fig. 2A, the experimental data (black) and the theoretical curves (red) obtained by global fitting analysis are plotted together for comparison and they show a good agreement. The solution scattering signal of interest is the difference between the signal measured at a positive time delay and the reference signal measured at the time delay of −3 ns that represents the scattering signal of the unexcited sample. To check if the timing between the laser and X-ray pulses is precisely set, the difference intensity was measured at t = −200 ps, giving approximately zero for all q values (data not shown). In contrast, for the data measured at positive time delays shown in Fig. 2A, the scattering curves are oscillatory around the q axis. These difference signals are the signatures of changes in the molecular structures during the chemical reaction.

To get a more intuitive picture of structural change in the reacting molecules, the scattering patterns $q\Delta S(q)$ were sine-Fourier-transformed into real space. The resultant difference radial distribution functions (RDF), $r\Delta S(r)$, where r is the atom–atom distance, are shown in Fig. 2B. The RDF signal is the change of radial electron density around an (averaged) excited atom as a function of the interactomic distance r, and represents the change of the atom–atom pair distrbution function during the course of the reaction. As can be seen in the $r\Delta S(r)$ data measured at t = 100 ps, two negative peaks (at 2.34 Å and 4.95 Å) and a positive peak (at 3.65 Å) are distinct. Intuitively, when considering the lengths of those atomic pairs in $HgBr_2$ from computed results (Table 1), the first negative peak is assigned to the Hg–Br bond breakage, and the second to the disappearance of the Br···Br correlation inside the parent molecule (where '···' indicates an interatomic pair). However, it is difficult to assign the peaks clearly for the measured raw signal in Fig. 2A and B because the solution scattering signal is a mixture of three components (solute-only, solvent-only and the solute–solvent cross-terms). To make more clear assignment, the difference signal can be decomposed to the three components, as shown in Fig. 2C–E. The decomposition was done after globally fitting the experimental

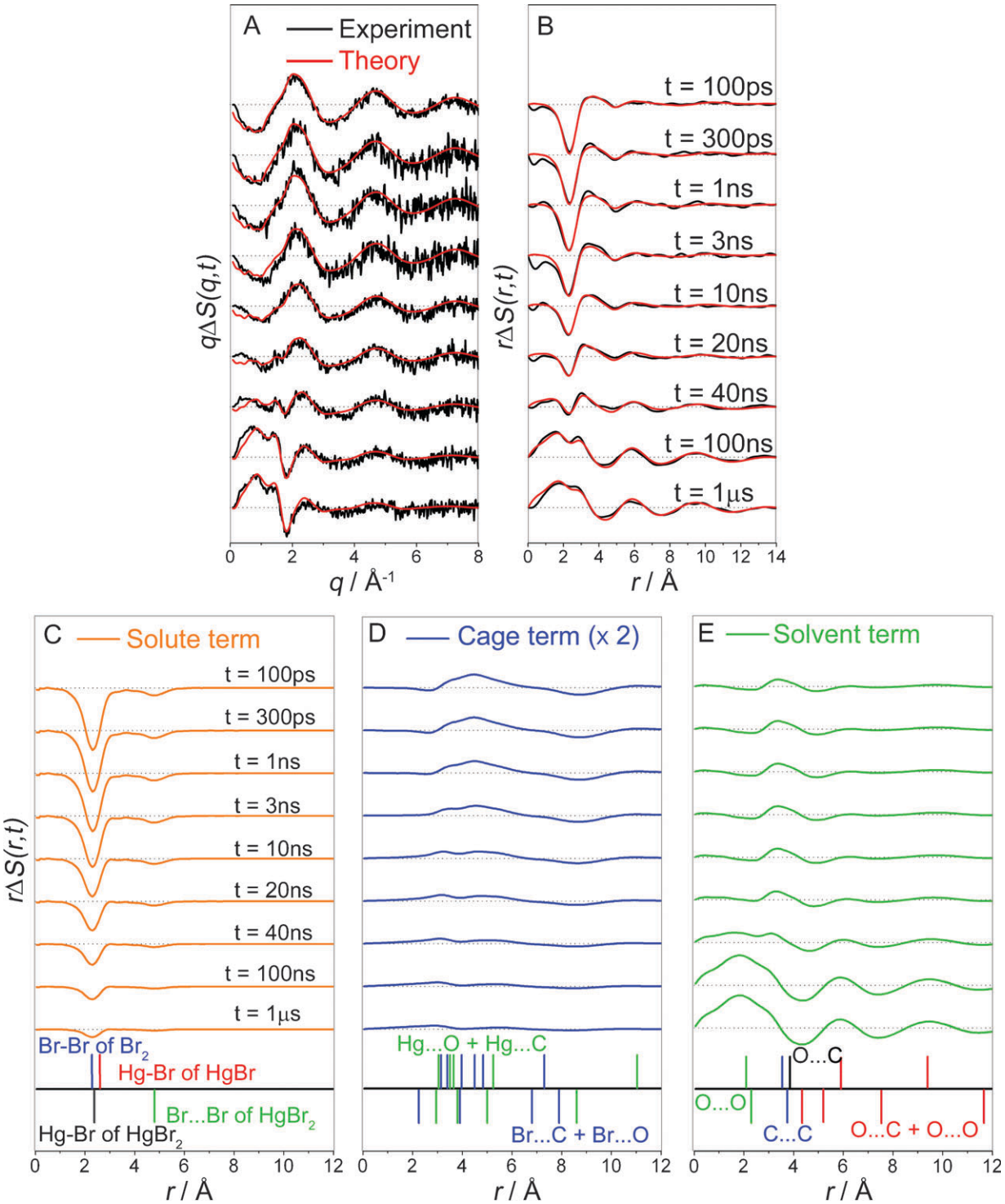

Fig. 2 TRXL signals from $HgBr_2$ in methanol at various time delays after photolysis at 267 nm. (A) Experimental (black) difference scattering curves represented as $q\Delta S(q)$ in q space and theoretical curves (red) obtained by global fitting analysis of the experimental data. (B) Difference RDFs, $r\Delta S(r)$, obtained by sine-Fourier transformation of the $q\Delta S(q)$ difference scattering curves in (A). The RDF signals are decomposed into three components: (C) the solute-only term, (D) the solute–solvent cross-term (cage term), and (E) the solvent-only term. In the bottom of Fig. 3C–E, the peak positions of the major contributions in each species are shown as lines. The lines in (C) indicate the bond lengths calculated by the DFT. The lines in (D) and (E) indicate the peak positions of solvent-related RDF terms calculated by MD simulation. The lines above the baseline contribute to positive features in the scattering curves, while the lines below the baseline contribute to negative features. Each contribution is color-coded for clarity. In (E), the features in the scattering data before 10 ns only arise from the temperature change, while those after 10 ns are mainly attributed to the ensuing decrease in density.

curves at all time delays by using a theoretical model function consisting of the three components, as described in eqn (8). By analyzing the changes in the amplitude and shape of these decomposed components, the origin of the difference scattering

Table 1 Theoretical structure parameters of HgX_2(X = Br, I) in methanol. All values were calculated by DFT with the PBE0 functional. Basis sets for Hg, Br and I were all aug-cc-pVTZ-PP RECP. The CPCM method was used to describe the methanol solvent effects

Channel	Hg–X (Å)	X–X (Å)	X–Hg–X (°)	Hg–X–X (°)
$HgBr_2$	2.405	4.810	180.00	—
HgBr–Br	2.573	2.600	—	180.00
HgBr + Br	2.625	—	—	—
Hg + Br_2	—	2.286	—	—
Hg + 2Br	—	—	—	—
HgI_2	2.587	5.174	180.00	
HgI–I	2.799	2.893	—	180.00
HgI + I	2.814	—	—	—
Hg + I_2	—	2.669	—	—
Hg + 2I	—	—	—	—

signal and related reaction dynamics can be well accounted for. The peaks and valleys in the difference curves in Fig. 2C–E are assigned with lines shown at the bottom. The lines represent the peak positions of theoretically generated RDFs for the chemical species involved in the reaction. Since each line has a different degree of broadening and contribution to the total RDF signal, individual lines might not exactly match the peaks and valleys of the difference curves in Fig. 2C–E.

In the solute-only term in Fig. 2C, the negative peaks at 2.40 Å and 4.85 Å decrease in amplitude as time evolves. As discussed above, these two peaks are the major signatures of the parent ($HgBr_2$) molecule, *i.e.* the Hg–Br bond and the Br···Br atomic pair correlation, respectively. The same features are observed in the raw scattering data as well, but they are more distinct in the solute-only term, where the solvent contribution is eliminated. In contrast, the signatures of an intermediate, the HgBr radical and a product (Br_2) appear as positive peaks but with much smaller intensities, mainly due to a partial overlap with the negative Hg–Br peak. As a result, they are barely visible even in the solute-only curves and only make the broad negative peak at 2.40 Å asymmetric.

From the solute–solvent cross-term in Fig. 2D, structural information about the solvent packing around the solutes, *i.e.* the solvent cage structure, can be obtained. In the cross-term in Fig. 2D, a broad positive peak at ~4.5 Å appears, while a negative peak is seen at ~8.7 Å. These features indicate that the distance between the solute and solvent molecules have decreased owing to the photodissociation of $HgBr_2$. The dissociation of Br atoms from the Hg atom facilitates the access of the solvent (methanol) molecules to Hg and Br, thus reducing the distance between solute and solvent molecules. The positive peak at ~3.64 Å in the raw difference scattering curve in Fig. 2B can also be explained by the structural changes in the cage and the change in solvent temperature, which will be discussed in the next paragraph.

From the solvent-only term in Fig. 2E, the heat dissipation and the solvent rearrangement induced by photodissociation can be obtained. To do so, the solvent signal can be further decomposed in q space into $q[\partial S(q)/\partial T]_V$ and $q[\partial S(q)/\partial \rho]_T$ terms. At early time delays (<10 ns), the $q[\partial S(q)/\partial T]_V$ term is responsible for the increase in temperature (and pressure) of the solvent at a constant volume, resulting in the broadening of the atom–atom distance distributions of O···O and O···C of adjacent methanol molecules. Then, after ~10 ns, $(q[\partial S(q)/\partial \rho]_T)$ accounts for the thermal expansion, leading to the equilibration to ambient pressure in a slightly expanded volume and therefore decreased density. As a result, the interatomic distance distributions of O···O and O···C in the solvent change, resulting in the highly oscillatory scattering curves observed after 100 ns.

3.2 Determination of reaction pathways

To determine the major reaction pathway in a more systematic way, we fit the experimental scattering signals to theoretical scattering curves from the four putative reaction pathways. The experimental data and theoretical scattering curves obtained from least-squares fitting are compared in Fig. 3A. Here we show only the 100 ps data, but the same holds for other time delays as the data at all time delays are fitted together in the global fitting analysis. The discrepancy between the experimental and theoretical curves can be evaluated by the reduced chi-square($\chi^2_{v,j}$) values defined by

$$\chi^2_{v,j} = \chi^2_j/(N - m)$$

where j is a given time delay, N is the number of data points along the q axis, and m is the number of fitting parameters. This $\chi^2_{v,j}$ is commonly used as a measure of the goodness of a fit, and $\chi^2_{v,j}$ value of 1 means the best fit.

As can be seen in Fig. 3A, the three-body dissociation into a Hg and two Br atoms, *i.e.* pathway (2), gives the best fit ($\chi^2_{v,\,100\,ps} = 1.76$) while the two-body dissociation into HgBr and Br, *i.e.* pathway (1), gives the second-best fit $\chi^2_{v,\,100\,ps} = 2.73$). In order to consider the possibility of branching between different reaction pathways, we used a theoretical curve combining all four reaction pathways to fit the experimental data. From the fitting using the combined pathways, the best fit ($\chi^2_{v,\,100\,ps} = 1.59$) was obtained when the reaction pathway consists of only pathways (1) and (2) with ~2 : 1 ratio with negligible contributions from pathways (3) and (4). Thus, the major reaction pathway of $HgBr_2$ photodissociation is determined to be branched between two-body and three-body dissociation pathways. Here, we note that the branched pathways (1) and (2) are not completely parallel to each other. In pathway (2), the three-body dissociation to Hg and Br atoms occurs, but the Hg and Br atoms subsequently recombine to form HgBr (Hg + Br → HgBr), opening a route between pathways (2) and (1). This conversion of Hg and Br atoms to HgBr clearly affects the reaction dynamics on the timescale longer than 100 ps reported in this work. Thus, it is the complex interplay of the various chemical species formed in the branched reaction pathways that constitutes the measured X-ray solution scattering pattern. Thanks to the wide q-range and the quality of the scattering data, we can extract such detailed information with the aid of theoretical tools and fitting analysis.

3.3 Dynamics of $HgBr_2$ photodissociation in methanol

The reaction dynamics can be extracted from the global fitting analysis of the data measured at various time delays. The time-dependent concentration, $c_k(t)$, of each species comprising the solute-only term in eqn (8) is provided by integrating the rate

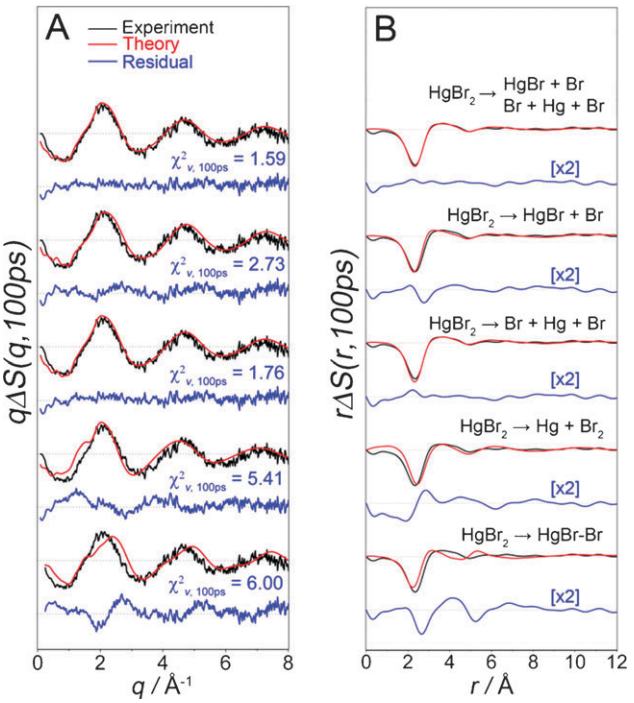

Fig. 3 Determination of the reaction pathways for $HgBr_2$ photodissociation in methanol. Experimental (black) and theoretical (red) difference scattering curves and their residual (blue) obtained by subtracting the theoretical curves from the experimental curves are shown in terms of (A) $q\Delta S(q)$ and (B) $r\Delta S(r)$. Here we show only the 100 ps data, but it is the result of global fitting analysis considering the data of all time delays. The $\chi^2_{v,\,100\,ps}$ values represent the discrepancy between the experimental and theoretical curves at 100 ps. The reaction channels consisting of two-body and three-body dissociation with a 2 : 1 ratio provides the best fit. The peak assignments are the same as in Fig. 2C–E.

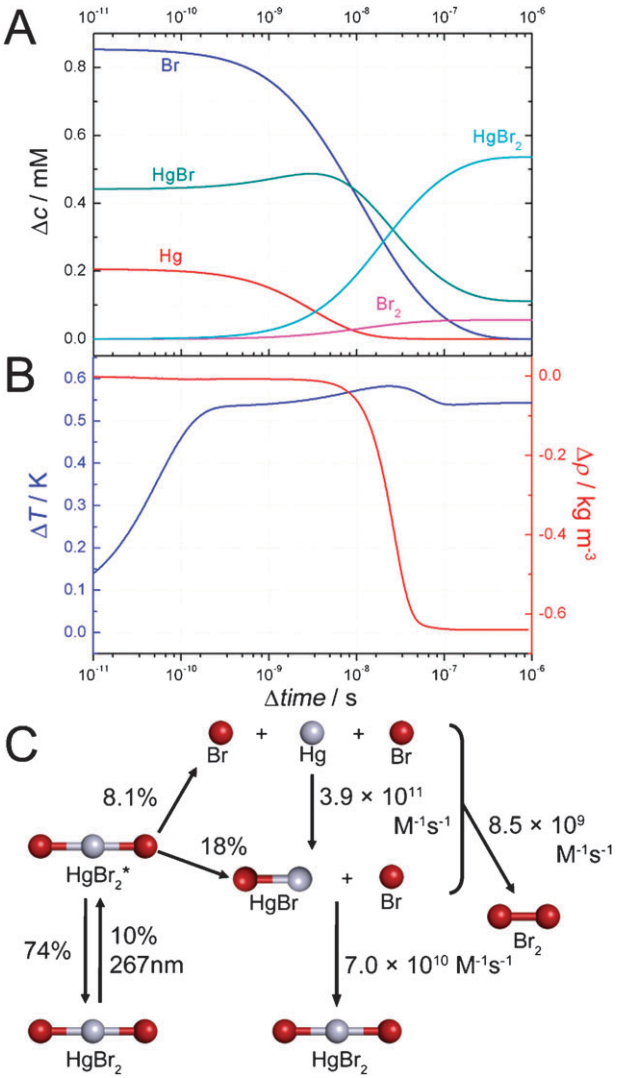

Fig. 4 (A) Time-dependent concentration changes of chemical species involved in the photodissociation reaction of $HgBr_2$ in methanol obtained from global-fitting analysis. Br (blue), HgBr (green), Hg (red), $HgBr_2$ (cyan), Br_2 (magenta). (B) Time-dependent changes of solvent temperature (blue) and density (red) induced by photodissociation of $HgBr_2$ obtained from the global-fitting analysis. (C) Schematic of the reaction mechanism of $HgBr_2$ photodissociation in methanol determined by the TRXL measurements and analysis.

equations for a set of selected chemical reactions. For the $HgBr_2$ photodissociation reaction, the time evolution of each chemical species involved in the reaction, *i.e.* Hg, Br, HgBr, Br_2, and $HgBr_2$, was extracted and plotted in Fig. 4A. By keeping track of the population changes of the reactant, intermediates and products species, the detailed structural dynamics and reaction rate of each step were elucidated. Initially, 10% of the $HgBr_2$ molecules in the 25 mM methanol solution are excited by the 266 nm laser pulse. Among the photoexcited $HgBr_2$* molecules, 74% decays into the ground state by electronic/vibrational relaxation or geminate recombination, releasing their energy to the solvent bath. The remaining 26% portion of $HgBr_2$* dissociate completely (8%) or stay as an HgBr radical (18%).

With both two-body and three-body dissociation, the chemical species present at 100 ps are HgBr, Br and Hg. Among them, Br is the dominant species since it is produced in both two-body and three-body dissociation. The transient Br atoms are consumed in three ensuing reactions. First, 24% of the generated Br atoms recombine with the entire population of Hg atoms to form HgBr radicals at a rate of 3.9×10^{11} M^{-1} s^{-1}, leading to the increase of HgBr population in 1–10 ns (see Fig. 4A). Secondly, 63% of the Br atoms recombine nongeminately with the HgBr radical at a rate of 7.0×10^{10} M^{-1} s^{-1} to form the parent $HgBr_2$ molecule. The remaining 13% of the Br atoms combine to form Br_2 at a rate of 8.5×10^9 M^{-1} s^{-1}, which is about two times lower than the recombination rate (1.5×10^{10} M^{-1} s^{-1}) of Br_2 in CCl_4 solution.[75,76]

Besides the population dynamics of the solutes, the dynamics of the heat dissipation induced by the reaction can be extracted from the solvent-only term in the scattering signal. The Fig. 4B shows the change in the solvent density and the solvent temperature, which correspond to to $\Delta\rho(t)$ and $\Delta T(t)$, respectively, in the solvent-only term in eqn (8). In the early stages of the reaction prior to 10 ns, the heat is dissipated at a constant volume, leading to the temperature rise of 0.54 K. After 10 ns thermal expansion occurs, resulting in a decrease in the density of methanol by 0.64 kg m^{-3} until 100 ns.

However, when considering the low concentration of the chemical species in the reaction, a temperature rise as small as 0.13 K is predicted from the reaction. The extra 0.41 K temperature rise is attributed to the heat dissipated from fast recovery to the $HgBr_2$ ground state by geminate recombination and vibrational cooling in the ground state. As mentioned above, only ~30% the photoexcited $HgBr_2$* molecules go through the dissociation pathway, while the rest relax back to the electronic ground state and dissipate their energy to the solvent bath *via* collisions with solvent molecules. Since such recovery processes to the ground state occur on the 10 ps timescale,[77] they were not resolved in our experiment.

3.4 Comparison with HgI_2 photodissociation

The results of this work on $HgBr_2$ can be compared with a previous TRXL study of another mercury halide system, HgI_2.[46] For comparison, the results from the X-ray solution scattering studies of the two mercuric halides are summarized in Table 2. Here, it should be noted that the rate constants of the HgI_2 photodissociation reported in the previous work[46] were all doubled by a miscoding of the fitting program. So in order to correct this analytical error, the rate constants listed in Table 2 were obtained by dividing the previously reported values by a factor of 2.

The efficiency of the $HgBr_2$ photoexcitation by ultraviolet laser pump is only 10% compared to 33% efficiency in HgI_2. Such difference in excitation efficiency is ascribed to higher absorption cross-section of HgI_2 than $HgBr_2$ at 266 nm, as can be seen in their absorption spectra in Fig. 5. In this study, the difference was compensated for by using a higher concentration of $HgBr_2$ (25 mM) than of HgI_2 (10 mM) used in the previous work. After photoexcitation, 74% of $HgBr_2$* returns to the ground state by geminate recombination compared to 66% of HgI_2*.

As can be seen in Table 2, the most notable difference between the photodissociation of $HgBr_2$ and HgI_2 is the branching ratio between two-body and three-body dissociation pathways. In other words, the photodissociation of HgI_2 occurs only *via* two-body dissociation pathway, whereas $HgBr_2$ dissociates *via* both two-body (18%) and three-body (8%) dissociation pathways with about a 2 : 1 branching ratio. The difference in the reaction pathways of the two mercuric halides demonstrates the effect of atomic substituents on the reaction mechanism in a simple chemical reaction, although its origin is not clear yet. We can speculate that three-body dissociation of HgI_2 occurs at a much higher rate than that of $HgBr_2$, for example at much earlier times than 100 ps. If so, the pathway might not observed with the 100 ps time resolution of this experiment.

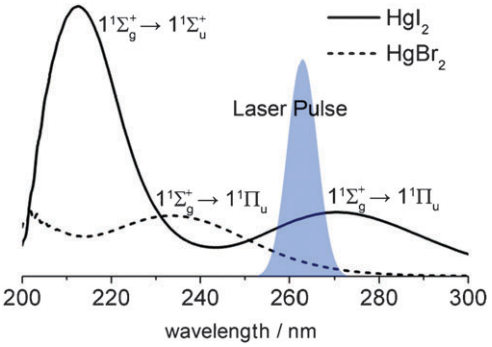

Fig. 5 Absorption spectra of HgI_2 (solid) and $HgBr_2$ (dashed) in methanol solution and the spectrum of excitation laser pulse used in the TRXL experiment.

The branching ratios and the recombination rates were also found to be different between $HgBr_2$ and HgI_2. In particular, *via* X + X → X_2 (X = Br, I) reaction, 13% of Br atoms combine to form Br_2 at 8.5×10^9 M^{-1} s^{-1} in contrast to the formation of I_2 with its 29% branching ratio and 1.7×10^{10} M^{-1} s^{-1}. The slower formation of Br_2 than I_2 disagrees with a previous spectroscopic study, where the nongeminate recombination of photodissociated Br_2 was found to be almost twice as fast as that of I_2 in CCl_4 solution.[76] This reversal in relative formation rates might be explained by our use of a polar solvent, methanol, rather than the nonpolar solvent CCl_4 used in the previous study, but the exact origin needs further investigation. In contrast, for HgX_2 recovery *via* the HgX + X → HgX_2 reaction, the reaction rate is higher for $HgBr_2$ than for HgI_2. The higher rate of $HgBr_2$ formation is likely to result from the higher diffusion rate of Br.

Table 2 Comparison of $HgBr_2$ and HgI_2 photodissociation in terms of kinetic parameters obtained from global fitting analysis of the TRXL data

	$HgBr_2$	HgI_2
Photoexcitation efficiency of HgX_2, $[HgX_2^*]_0/[HgX_2]_{ground}$ [a]	10%	33%
Branching ratio of ground state recovery, HgX_2, $[HgX_2^*]_{relaxation}/[HgX_2^*]_0$ [a]	74%	66%
Branching ratio of two-body dissociation, HgX_2, $[HgX_2^*]_{two\text{-}body}/[HgX_2^*]_0$ [a]	18%	34%
Branching ratio of three-body dissociation, HgX_2, $[HgX_2^*]_{three\text{-}body}/[HgX_2^*]_0$ [a]	8%	~0%
Branching ratio of HgBr formation, Hg + Br → HgBr, from dissociated halogen atoms, $[X]_{Hg+X}/[X]_0$ [b] (and its rate constant)	24% (3.9×10^{11} M^{-1} s^{-1})	N/A
Branching ratio of HgX_2 recovery, HgX + X → HgX_2 (X = Br, I), from dissociated halogen atoms, $[X]_{HgX+X}/[X]_0$ [b] (and its rate constant)	63% (7.0×10^{10} M^{-1} s^{-1})	71% (5.0×10^{10} M^{-1} s^{-1})
Branching ratio of X_2 formation, X + X → X_2 (X = Br, I), from dissociated halogen atoms, $[X]_{X+X}/[X]_0$ [b] (and its rate constant)	13% (8.5×10^9 M^{-1} s^{-1})	29% (1.7×10^{10} M^{-1} s^{-1})

[a] By photoexcitation, HgX_2 is excited from the ground state to the electronic excited state, HgX_2*, with an initial population of $[HgX_2^*]_0$. The HgX_2* population decays *via* three pathways: (1) return to the ground state by electronic/vibrational relaxation and geminate recombination, $[HgX_2^*]_{relaxation}$, (2) dissociation into two bodies, $[HgX_2^*]_{two\text{-}body}$, or (3) dissociation into three bodies, $[HgX_2^*]_{three\text{-}body}$. [b] The halogen atoms (Br or I) dissociated from HgX_2* with an initial concentration of $[X]_0$ are consumed in three ensuing reactions: (1) recombination with Hg to form the HgX radical, $[X]_{Hg+X}$, (2) recombination with HgX to form HgX_2, $[X]_{HgX+X}$, or (3) combination with another halogen atom to form an X_2 molecule, $[X]_{X+X}$.

3.5 Error analysis

The reported reaction rate constants and branching ratios were calculated using the MINUIT software package by applying chi-square minimization fitting procedure, which is also known as maximum likelihood estimation (MLE). Here we note that the likelihood (L) is related to the chi-square (χ^2) by $L \propto \exp(-\chi^2/2)$. In this section, we discuss how we estimate the errors of multiple fit parameters used in the MLE fitting so that we can check the quality of our fitting results. In general, in MLE fitting with multiple fit parameters, the error estimate is made as follows.[78,79] First, the distribution of likelihood is obtained by varying the parameters from their optimized values, where χ^2 is minimized (and thus the likelihood is maximized). Then, the error range of each parameter is defined by one-standard-deviation confidence region that

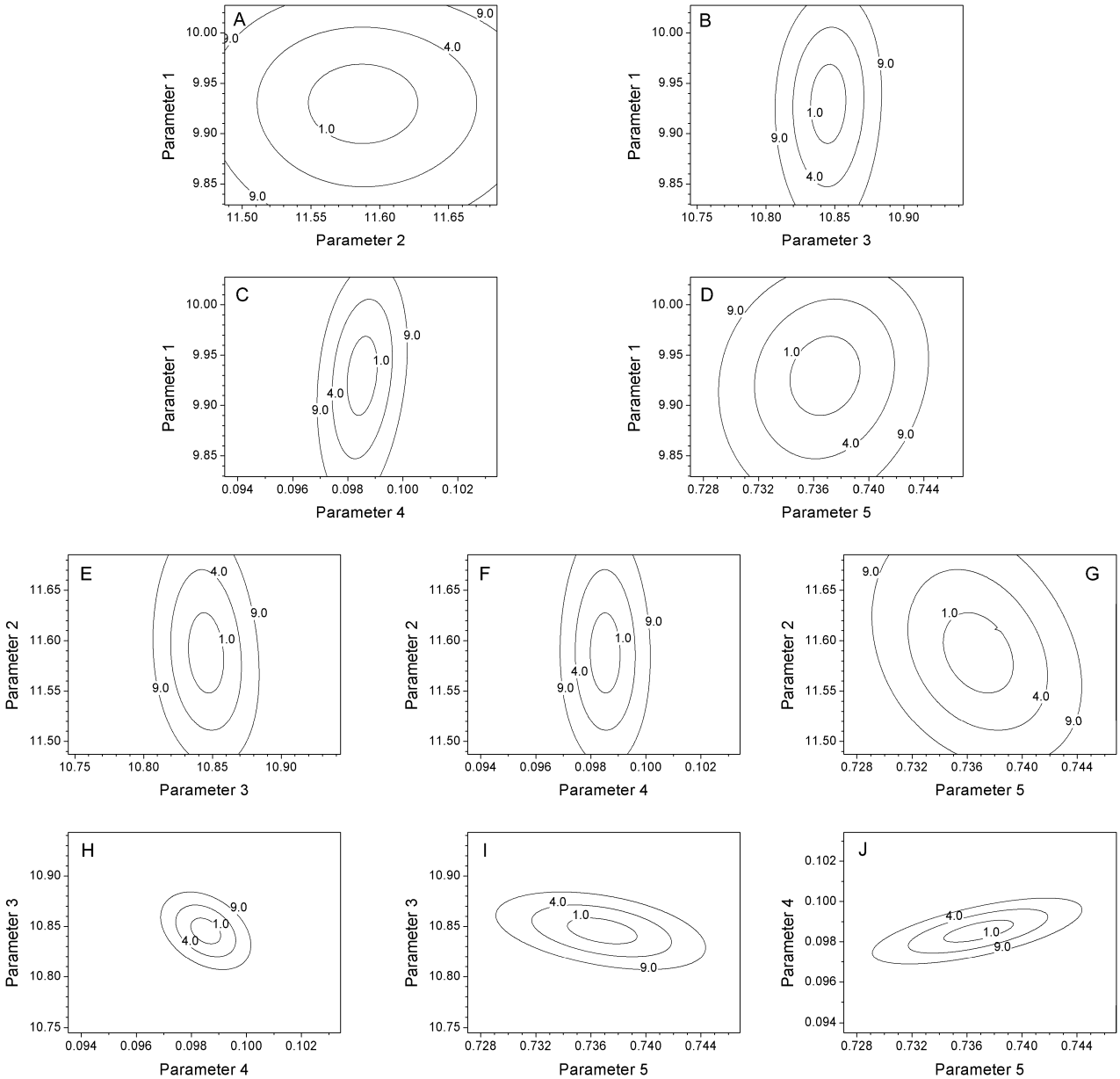

Fig. 6 Contour maps showing the variation of the adjusted χ^2 (*i.e.* $\Delta\chi^2 = \chi^2 - \chi^2_{min}$) with respect to a pair of correlated parameters among the five parameters used in the global fitting analysis. The errors were calculated manually by using our own code based on the MLE fitting method. The region within the boundaries of $\Delta\chi^2 = 1.0$, 4.0 and 9.0 corresponds to the likelihood distribution of 68.3%, 95% and 99.7%, respectively. The parameters 1 (Br + Br → Br_2), 2 (Hg + Br → HgBr) and 3 (HgBr + Br → $HgBr_2$) correspond to the rate constants (k) of various reaction pathways and are presented as the logarithm of each parameter to the base 10. Parameter 4 is the photoexcitation efficiency of $HgBr_2$, that is, $[HgBr_2^*]_0/[HgBr_2]_{ground}$. Parameter 5 is the branching ratio of ground state recovery, $[HgX_2^*]_{relaxation}/[HgX_2^*]_0$, *via* electronic/vibrational relaxation and geminate recombination. The negative error limit of parameter 1 was not available. In panels G, I and J, it can be seen that there exists a strong correlation between the two constituent parameters. The MINOS algorithm in MINUIT employed in our global fitting analysis automatically provides errors corresponding to boundary values of 68.3% of likelihood distribution, and thus this manual inspection of contour maps is not necessary to estimate errors based on likelihood distribution. Here we show these contour maps for demonstration purposes.

Table 3 Comparison of error values from MIGRAD, HESSE and MINOS subroutines provided by the MINUIT minimization software used in the global fitting analysis. To confirm that MINOS gives errors based on the likelihood distribution, we also manually estimated the errors using the boundary values of 68.3% of likelihood distribution

		Error Value			
		MINUIT			
	Value	MIGRAD	HESSE	MINOS	68.3% of likelihood distribution
Rate constant of Br + Br → Br_2 [a]	9.93	±0.057	±0.040	±0.040	−0.040/+0.039
Rate constant of Hg + HgBr → HgB_2 [a]	11.59	±0.26	±0.040	±0.040	−0.039/+0.041
Rate constant of HgBr + Br → $HgBr_2$ [a]	10.83	±0.071	±0.013	±0.013	−0.013/+0.013
Photoexcitation efficiency of $HgBr_2$, $[HgBr_2^*]_0/[HgBr_2]_{ground}$	10 (%)	±0.24	±0.055	±0.055	−0.054/+0.055
Branching ratio of ground state recovery, $[HgX_2^*]_{relaxation}/[HgX_2^*]_0$	74 (%)	±1.3	±0.25	±0.25	−0.25/+0.25

[a] The presented values are obtained by taking the logarithm of each rate constant and error value to the base 10. The unit of the original values is M^{-1} s^{-1}.

corresponds to the region within 68.3% range of the determined likelihood distribution. In this work, nine parameters were used in the MLE fitting of the data, but only five of them were used for the error analysis. The other four parameters mostly account for the dynamics on the timescale shorter than the time resolution of our experiment and thus are not appropriate for error analysis. To account for nonlinearities and correlations between the fit parameters, we represented the χ^2 function in a five-dimensional space consisting of those five parameters. Fig. 6 shows five-dimensional space sliced to ten contour maps. Each contour map shows the variation of $\Delta\chi^2$ with respect to a pair of correlated parameters, where $\Delta\chi^2$ is the adjusted χ^2 by subtracting the minimum χ^2 value from the χ^2 value at a certain position in the contour map (*i.e.* $\Delta\chi^2 = \chi^2 - \chi^2_{min}$). For each parameter, the probability that the true value of a parameter lies inside the $\Delta\chi^2 = 1$ boundary is 68.3%. Therefore, the parameter values at the $\Delta\chi^2 = 1$ boundary gives an estimate of the error range for each parameter. The same approach was followed by Nielsen and coworkers, who manually estimated the errors by using coutour maps.[53,54] Here we point out that the same error estimation based on this principle is automatically provided in the MINUIT software that has been used in our global fitting analysis.[43–45]

The MINUIT software provides three algorithms (MIGRAD, HESSE and MINOS) to estimate errors of the parameters determined from MLE fitting. The MIGRAD performs a function minimization using the gradient (or curvature) of the χ^2 function. As the gradient converges to the value at the minimum, the error matrix calculated at each point converges to a correct form. The HESSE also makes use of the curvature of the χ^2 function, but it initially calculates the full matrix of the second-derivatives (*i.e.* curvature) of the χ^2 function (by finite intervals) with respect to the variable parameters and inverting the matrix to produce an error matrix. Therefore, compared to MIGRAD where the initial value of the χ^2 minimization loop can play a critical role, the HESSE can give a more accurate error range and account for the effects due to correlations between multiple parameters. However, both MIGRAD and HESSE assume that the χ^2 function is of parabolic shape around the minimum and thus they do not work well in the presence of high nonlinearities in the χ^2 function. Instead of seeking to converge the curvature to a minimum, MINOS makes use of the likelihood distribution starting from the minimum to estimate the error, as described in the previous paragraph. Therfore, MINOS is the most relevant method for highly nonlinear problems as well as for handling errors of correlated multiple parameters used in the global fitting analysis.[63] In our results, the χ^2 function is not highly nonlinear, resulting in identical error values from the HESSE and MINOS (see Table 3).

For comparison, we also calculated the errors manually by using our own code based on MLE fitting, as listed in the last column of Table 3. We note that the $\Delta\chi^2$ contour maps shown in Fig. 6 could also be obtained from this manual error analysis. It is clearly seen that the errors obtained by this manual calculation are very close to those calculated by MINOS. This comparison clearly demonstrates that the error estimate by the MINOS algorithm in the MINUIT software is equivalent to the manual MLE error analysis that was recently highlighted.[53,54]

4. Conclusion

We have measured the photodissociation dynamics of $HgBr_2$ from 100 ps to 1 μs using time-resolved X-ray liquidography. By monitoring the reaction dynamics, spanning four orders of magnitude in time, the recombination dynamics of the photodissociated species and the energy dissipation from the reacting species to the solvent molecules were elucidated. Also, the reaction pathways and detailed mechanism of $HgBr_2$ photodissociation were revealed. In particular, the major reaction pathway of $HgBr_2$ photodissociation consists of both two-body and three-body dissociation pathways, in contrast to HgI_2 that dissociates through two-body dissociation only within the currently available time resolution of ~100 ps.

Acknowledgements

This work was supported by the Creative Research Initiative (Center for Time-Resolved Diffraction) of MEST/NRF.

References

1 R. O. Pierce, *Wied. Ann.*, 1879, **6**, 597.
2 J. Maya, *J. Chem. Phys.*, 1977, **67**, 4976–4980.
3 B. E. Wilcomb, R. Burnham and N. Djeu, *Chem. Phys. Lett.*, 1980, **75**, 239–242.
4 A. Gedanken, B. Raz, U. Even and I. Eliezer, *J. Mol. Spectrosc.*, 1969, **32**, 287.

5 S. Bell, R. D. McKenzie and J. B. Coon, *J. Mol. Spectrosc.*, 1966, **20**, 217.
6 C. Whitehurst and T. A. King, *J. Phys. D: Appl. Phys.*, 1987, **20**, 1577.
7 W. R. Wadt, *J. Chem. Phys.*, 1980, **72**, 2469–2478.
8 V. Kushawaha and M. Mahmood, *J. Appl. Phys.*, 1987, **62**, 2173–2177.
9 V. Kushawaha, A. Michael and M. Mahmood, *J. Phys. B: At., Mol. Opt. Phys.*, 1988, **21**, 2507.
10 R. Azria, J. P. Ziesel, R. Abouaf, L. Bouby and M. Tronc, *J. Phys. B: At. Mol. Phys.*, 1983, **16**, L7.
11 J. Husain, J. R. Wiesenfeld and R. N. Zare, *J. Chem. Phys.*, 1980, **72**, 2479–2483.
12 J. J. A. McGarvey, N.-H. Cheung, A. C. Erlandson and T. A. Cool, *J. Chem. Phys.*, 1981, **74**, 5133–5142.
13 J. Maya, *IEEE J. Quantum Electron.*, 1979, **15**, 579–594.
14 G. A. Bowmaker, *Spectroscopy of inorganic-based materials*, Wiley, New York, 1987.
15 A. C. Erlandson and T. A. Cool, *Chem. Phys. Lett.*, 1983, **96**, 685–689.
16 R. M. Bowman, M. Dantus and A. H. Zewail, *Chem. Phys. Lett.*, 1989, **156**, 131–137.
17 M. Dantus, R. M. Bowman, M. Gruebele and A. H. Zewail, *J. Chem. Phys.*, 1989, **91**, 7437–7450.
18 T. Baumert, S. Pedersen and A. H. Zewail, *J. Phys. Chem.*, 1993, **97**, 12447–12459.
19 D. P. Zhong and A. H. Zewail, *J. Phys. Chem. A*, 1998, **102**, 4031–4058.
20 K. B. Moller and A. H. Zewail, *Chem. Phys. Lett.*, 1998, **295**, 1–10.
21 J. Somloi and D. J. Tannor, *J. Phys. Chem.*, 1995, **99**, 2552–2560.
22 J. H. Parks, *Appl. Phys. Lett.*, 1977, **31**, 192–194.
23 E. J. Schimitschek and J. E. Celto, *Opt. Lett.*, 1978, **2**, 64–66.
24 W. R. Wadt, *Appl. Phys. Lett.*, 1979, **34**, 658–660.
25 K. S. Viswanathan and J. Tellinghuisen, *J. Mol. Spectrosc.*, 1983, **98**, 185.
26 J. Tellinghuisen and J. G. Ashmore, *Appl. Phys. Lett.*, 1982, **40**, 867.
27 J. Tellinghuisen, P. C. Tellinghuisen, S. A. Davises, P. Berwanger and K. S. Viswanathan, *Appl. Phys. Lett.*, 1982, **41**, 789.
28 C. Salter, P. C. Tellinghuisen, J. G. Ashmore and J. Tellinghuisen, *J. Mol. Spectrosc.*, 1986, **120**, 334.
29 A. K. Rai and V. B. Singh, *Indian J. Phys.*, 1987, **61B**, 522.
30 N. H. Cheung and T. A. Cool, *J. Quant. Spectrosc. Radiat. Transfer*, 1979, **21**, 397.
31 T. D. Dreiling and D. W. Setser, *J. Chem. Phys.*, 1983, **79**, 5423.
32 D. P. Greene, K. P. Kileen and J. G. Eden, *J. Opt. Soc. Am. B*, 1986, **3**, 1282.
33 S. Gnanakaran and R. M. Hochstrasser, *J. Chem. Phys.*, 1996, **105**, 3486–3496.
34 S. Gnanakaran and R. M. Hochstrasser, *Int. J. Quantum Chem.*, 1999, **72**, 451–462.
35 S. Gnanakaran, M. Lim, N. Pugliano, M. Volk and R. M. Hochstrasser, *J. Phys.: Condens. Matter*, 1996, **8**, 9201–9220.
36 M. H. Lim, M. F. Wolford, P. Hamm and R. M. Hochstrasser, *Chem. Phys. Lett.*, 1998, **290**, 355–362.
37 N. Pugliano, S. Gnanakaran and R. M. Hochstrasser, *J. Photochem. Photobiol., A*, 1996, **102**, 21–28.
38 N. Pugliano, D. K. Palit, A. Z. Szarka and R. M. Hochstrasser, *J. Chem. Phys.*, 1993, **99**, 7273–7276.
39 N. Pugliano, A. Z. Szarka, S. Gnanakaran, M. Triechel and R. M. Hochstrasser, *J. Chem. Phys.*, 1995, **103**, 6498–6511.
40 N. Pugliano, A. Z. Szarka and R. M. Hochstrasser, *J. Chem. Phys.*, 1996, **104**, 5062–5079.
41 M. Volk, S. Gnanakaran, E. Gooding, Y. Kholodenko, N. Pugliano and R. M. Hochstrasser, *J. Phys. Chem. A*, 1997, **101**, 638–643.
42 H. Bursing and P. Vohringer, *Phys. Chem. Chem. Phys.*, 2000, **2**, 73–82.
43 H. Ihee, *Acc. Chem. Res.*, 2009, **42**, 356–366.
44 T. K. Kim, J. H. Lee, M. Wulff, Q. Y. Kong and H. Ihee, *ChemPhysChem*, 2009, **10**, 1958–1980.
45 H. Ihee, M. Lorenc, T. K. Kim, Q. Y. Kong, M. Cammarata, J. H. Lee, S. Bratos and M. Wulff, *Science*, 2005, **309**, 1223–1227.
46 T. K. Kim, M. Lorenc, J. H. Lee, M. Russo, J. Kim, M. Cammarata, Q. Y. Kong, S. Noel, A. Plech, M. Wulff and H. Ihee, *Proc. Natl. Acad. Sci. U. S. A.*, 2006, **103**, 9410–9415.
47 Q. Y. Kong, J. H. Lee, A. Plech, M. Wulff, H. Ihee and M. H. J. Koch, *Angew. Chem., Int. Ed.*, 2008, **47**, 5550–5553.
48 Q. Y. Kong, M. Wulff, J. H. Lee, S. Bratos and H. Ihee, *J. Am. Chem. Soc.*, 2007, **129**, 13584–13591.
49 J. H. Lee, J. Kim, M. Cammarata, Q. Kong, K. H. Kim, J. Choi, T. K. Kim, M. Wulff and H. Ihee, *Angew. Chem., Int. Ed.*, 2008, **47**, 1047–1050.
50 J. H. Lee, T. K. Kim, J. Kim, Q. Kong, M. Cammarata, M. Lorenc, M. Wulff and H. Ihee, *J. Am. Chem. Soc.*, 2008, **130**, 5834.
51 J. Davidsson, J. Poulsen, M. Cammarata, P. Georgiou, R. Wouts, G. Katona, F. Jacobson, A. Plech, M. Wulff, G. Nyman and R. Neutze, *Phys. Rev. Lett.*, 2005, **94**, 245503.
52 R. Neutze, R. Wouts, S. Techert, J. Davidsson, M. Kocsis, A. Kirrander, F. Schotte and N. Wulff, *Phys. Rev. Lett.*, 2001, **87**, 195508.
53 M. Christensen, K. Haldrup, K. Bechgaard, R. Feidenhans'l, Q. Y. Kong, M. Cammarata, M. Lo Russo, M. Wulff, N. Harrit and M. M. Nielsen, *J. Am. Chem. Soc.*, 2009, **131**, 502–508.
54 K. Haldrup, M. Christensen, M. Cammarata, Q. Kong, M. Wulff, Simon O. Mariager, K. Bechgaard, R. Feidenhans'l, N. Harrit and Martin M. Nielsen, *Angew. Chem., Int. Ed.*, 2009, **48**, 4180–4184.
55 A. Plech, V. Kotaidis, K. Istomin and M. Wulff, *J. Synchrotron Radiat.*, 2007, **14**, 288–294.
56 A. Plech, V. Kotaidis, A. Siems and M. Sztucki, *Phys. Chem. Chem. Phys.*, 2008, **10**, 3888–3894.
57 A. Henkel, O. Schubert, A. Plech and C. Sonnichsen, *J. Phys. Chem. C*, 2009, **113**, 10390–10394.
58 M. Cammarata, M. Levantino, F. Schotte, P. A. Anfinrud, F. Ewald, J. Choi, A. Cupane, M. Wulff and H. Ihee, *Nat. Methods*, 2008, **5**, 881–886.
59 S. Ahn, K. H. Kim, Y. Kim, J. Kim and H. Ihee, *J. Phys. Chem. B*, 2009, **113**, 13131–13133.
60 M. Andersson, E. Malmerberg, S. Westenhoff, G. Katona, M. Cammarata, A. B. Wöhri, L. C. Johansson, F. Ewald, M. Eklund, M. Wulff, J. Davidsson and R. Neutze, *Structure*, 2009, **17**, 1265–1275.
61 M. Wulff, A. Plech, L. Eybert, R. Randler, F. Schotte and P. Anfinrud, *Faraday Discuss.*, 2003, **122**, 13–26.
62 A. Plech, M. Wulff, S. Bratos, F. Mirloup, R. Vuilleumier, F. Schotte and P. A. Anfinrud, *Phys. Rev. Lett.*, 2004, **92**, 125505.
63 F. James and M. Roos, *Comput. Phys. Commun.*, 1975, **10**, 343–367.
64 M. Cammarata, M. Lorenc, T. K. Kim, J. H. Lee, Q. Y. Kong, E. Pontecorvo, M. Lo Russo, G. Schiro, A. Cupane, M. Wulff and H. Ihee, *J. Chem. Phys.*, 2006, **124**, 124504.
65 C. Adamo and V. Barone, *J. Chem. Phys.*, 1999, **110**, 6158–6170.
66 M. J. Frisch, G. W. Trucks, H. B. Schlegel, G. E. Scuseria, M. A. Robb, J. R. Cheeseman, J. A. Montgomery, T. V. Jr., K. N. Kudin, J. C. Burant, J. M. Millam, S. S. Iyengar, J. Tomasi, V. Barone, B. Mennucci, M. Cossi, G. Scalmani, N. Rega, G. A. Petersson, H. Nakatsuji, M. Hada, M. Ehara, K. Toyota, R. Fukuda, J. Hasegawa, M. Ishida, T. Nakajima, Y. Honda, O. Kitao, H. Nakai, M. Klene, X. Li, J. E. Knox, H. P. Hratchian, J. B. Cross, V. Bakken, C. Adamo, J. Jaramillo, R. Gomperts, R. E. Stratmann, O. Yazyev, A. J. Austin, R. Cammi, C. Pomelli, J. W. Ochterski, P. Y. Ayala, K. Morokuma, G. A. Voth, P. Salvador, J. J. Dannenberg, V. G. Zakrzewski, S. Dapprich, A. D. Daniels, M. C. Strain, O. Farkas, D. K. Malick, A. D. Rabuck, K. Raghavachari, J. B. Foresman, J. V. Ortiz, Q. Cui, A. G. Baboul, S. Clifford, J. Cioslowski, B. B. Stefanov, G. Liu, A. Liashenko, P. Piskorz, I. Komaromi, R. L. Martin, D. J. Fox, T. Keith, M. A. Al-Laham, C. Y. Peng, A. Nanayakkara, M. Challacombe, P. M. W. Gill, B. Johnson, W. Chen, M. W. Wong, C. Gonzalez and J. A. Pople, *GAUSSIAN 03 (Revision E.01)*, Gaussian, Inc., Wallingford, CT, 2004.
67 M. Hargittai, *Chem. Rev.*, 2000, **100**, 2233–2302.
68 K. A. Peterson and C. Puzzarini, *Theor. Chem. Acc.*, 2005, **114**, 283–296.
69 K. A. Peterson, D. Figgen, E. Goll, H. Stoll and M. Dolg, *J. Chem. Phys.*, 2003, **119**, 11113–11123.

70 K. A. Peterson, B. C. Shepler, D. Figgen and H. Stoll, *J. Phys. Chem. A*, 2006, **110**, 13877–13883.
71 M. Cossi, N. Rega, G. Scalmani and V. Barone, *J. Comput. Chem.*, 2003, **24**, 669–681.
72 K. Refson, *Comput. Phys. Commun.*, 2000, **126**, 310–329.
73 M. Haughney, M. Ferrario and I. R. Mcdonald, *J. Phys. Chem.*, 1987, **91**, 4934–4940.
74 W. G. Hoover, *Phys. Rev. A: At., Mol., Opt. Phys.*, 1985, **31**, 1695–1697.
75 R. L. Strong, *J. Am. Chem. Soc.*, 1965, **87**, 3563–3567.
76 Z. R. Zhu and J. M. Harris, *Chem. Phys. Lett.*, 1991, **186**, 183–188.
77 W. M. Kwok, C. S. Ma, A. W. Parker, D. Phillips, M. Towrie, P. Matousek and D. L. Phillips, *J. Chem. Phys.*, 2000, **113**, 7471–7478.
78 W. H. Press, S. A. Teuolsky, W. T. Vetterling and B. P. Flannery, *Numerical recipes in C++, The art of scientific computing*, Cambridge University Press, Cambridge, 2nd edn, 2002.
79 P. R. Bevington and D. K. Robinson, *Data reduction and error analysis for the physical sciences*, McGraw-Hill, New York, 3rd edn, 2003.